

Enhancing Blind Face Restoration through Online Reinforcement Learning

Bin Wu^{1,2}, Yahui Liu³, Chi Zhang^{1,2}, Yao Zhao^{1,2}, Wei Wang^{1,2*}

¹Institute of Information Science, Beijing Jiaotong University

²Visual Intelligence +X International Cooperation Joint Laboratory of MOE

³Kuaishou Technology

Abstract

Blind Face Restoration (BFR) encounters inherent challenges in exploring its large solution space, leading to common artifacts like missing details and identity ambiguity in the restored images. To tackle these challenges, we propose a Likelihood-Regularized Policy Optimization (LRPO) framework, the first to apply online reinforcement learning (RL) to the BFR task. LRPO leverages rewards from sampled candidates to refine the policy network, increasing the likelihood of high-quality outputs while improving restoration performance on low-quality inputs. However, directly applying RL to BFR creates incompatibility issues, producing restoration results that deviate significantly from the ground truth. To balance perceptual quality and fidelity, we propose three key strategies: 1) a composite reward function tailored for face restoration assessment, 2) ground-truth guided likelihood regularization, and 3) noise-level advantage assignment. Extensive experiments demonstrate that our proposed LRPO significantly improves the face restoration quality over baseline methods and achieves state-of-the-art performance.

1. Introduction

Blind Face Restoration (BFR), which aims to reconstruct high-quality (HQ) faces from low-quality (LQ) inputs with unknown degradations, has made rapid progress in recent years. Modern BFR methods typically exploit various types of priors to establish direct mappings from LQ to HQ. These priors can be categorized into several types: (1) *geometric priors* (e.g., facial landmarks [7, 18], parsing maps [5], and component heatmaps [46]) that provide structural guidance; (2) *generative priors* [4, 36, 44] derived from pre-trained models such as StyleGAN [14, 15], which enable realistic detail reconstruction; (3) *discrete codebook priors* [9, 52] improve restoration fidelity; and (4) *diffusion priors* [6, 21, 39, 41, 48] is built upon the denoising and noise-adding diffusion model. Diffusion models offer distinct advantages

including robust generative capability, stable optimization, and superior control over output diversity, making them particularly effective for producing high-quality, visually pleasing face restorations.

However, despite the advantages of diffusion priors, BFR remains fundamentally challenging. The task is an ill-posed inverse problem where a single LQ input can be corresponded to multiple plausible HQ solutions, making it difficult to determine the optimal restoration. Current methods are constrained by their deterministic nature. They learn a fixed one-to-one mapping that produces a single output without considering alternative solutions. This lack of exploration within the vast solution space prevents these methods from discovering potentially superior restorations, leading to suboptimal results [51].

To address these exploration limitations, we propose incorporating reinforcement learning (RL) into BFR. RL has demonstrated remarkable success across various domains, particularly in language models [29, 45] and vision models [8, 22, 35, 47], by enabling diverse exploration strategies rather than deterministic outputs. Building on recent advances that successfully integrate RL with diffusion models [22, 42]—where the denoising process is formulated as a Markov decision process—we leverage RL’s exploration capabilities alongside diffusion models’ inherent randomness to systematically search BFR’s solution space for optimal restorations that enhance both fidelity and perceptual quality.

To this end, we introduce the first online RL framework to BFR: Likelihood-Regularized Policy Optimization (LRPO). Our framework utilizes a policy network to generate multiple diverse HQ candidate faces from each LQ input, effectively exploring the solution space rather than following a single deterministic trajectory. As shown in Figure 1 (left), this multi-candidate sampling strategy allows systematic exploration of potential solutions. A reward function evaluates each candidate, and relative advantages computed among candidates from the same input guide the policy network optimization. Moreover, we introduce three key innovations to enable effective RL optimization: (1) We design a composite reward function that evaluates restoration quality by incor-

*Corresponding author.

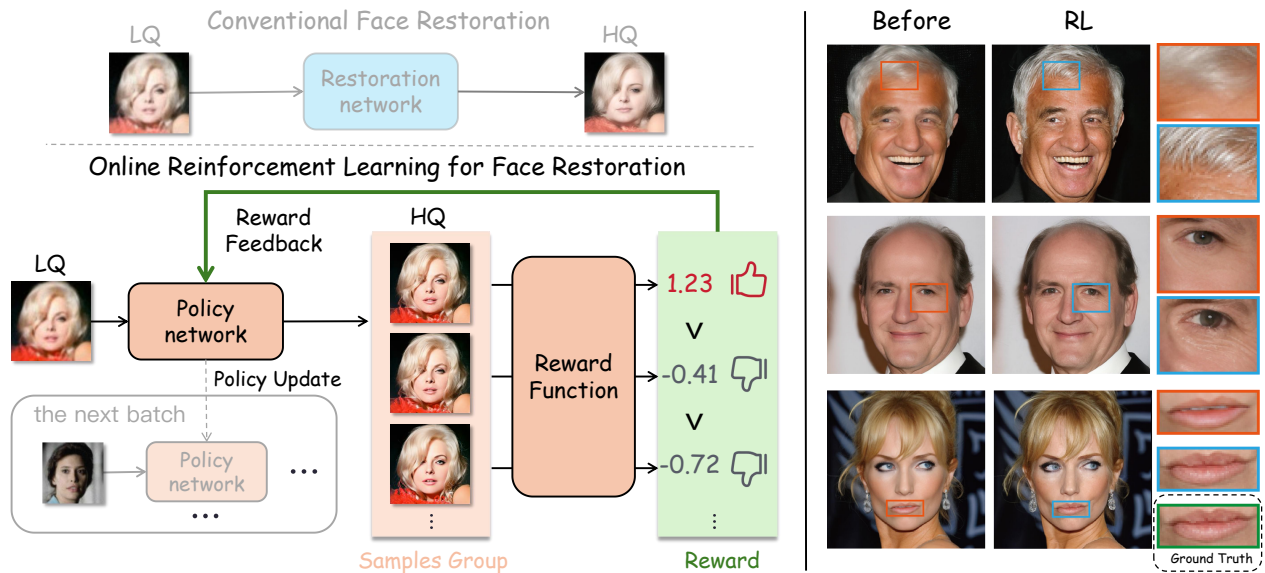


Figure 1. (Left) Our proposed online RL-based face restoration framework: an LQ face is input to the policy network π_θ , which generates a group of HQ face candidates. The reward function evaluates each candidate and converts the scores into within-group relative advantages that guide policy optimization for the next iteration. The comparisons (Right) demonstrate the quality improvement achieved through RL optimization over the base model.

porating human preferences, perceptual quality, and fidelity metrics. (2) To prevent reward hacking [1, 30]—where the policy exploits reward signals while deviating from authentic facial distributions—we implement ground-truth (GT) guided likelihood regularization that anchors the policy to the true data manifold. (3) We propose a noise-level advantage assignment mechanism that weights the advantages according to the importance of each denoising step, ensuring more effective policy updates.

In summary, our main contributions are as follows:

- We introduce online RL to BFR for the first time, modeling the learning process as exploration for superior restoration solutions. Specifically, we propose an LRPO framework that overcomes the limitations of single deterministic trajectory generation by exploring multiple restoration candidates through the RL training.
- We introduce three critical components for our proposed LRPO framework: a multi-faceted reward function that captures diverse restoration quality aspects, GT guided likelihood regularization that maintains authentic facial distributions while preventing reward exploitation, and adaptive advantage weighting that optimizes learning across different denoising stages.
- Our LRPO framework delivers substantial improvements in face restoration quality and establishes new *state-of-the-art* performance on standard evaluation metrics.

2. related work

Diffusion-based Blind Face Restoration. Blind Face Restoration (BFR) aims to recover high-quality face images from these degraded inputs while preserving identity consistency and perceptual quality. Recently, diffusion models [12, 31] have gained popularity due to their generative diversity and training stability. DR2 [39] uses a diffusion model for degradation removal, followed by refinement through an enhancement module. DifFace [48] constructs a posterior distribution to map LQ images to HQ counterparts, utilizing the error-shrinkage property of pre-trained diffusion models for robust restoration. To accelerate training, LDM [27] recommends training diffusion in the latent space. DiffBIR [21], built on LDM, employs ControlNet to guide restoration using low-quality faces as control signals. Some variations of diffusion models have been used for face restoration. InterLCM [20] leverages the latent consistency model (LCM) to improve semantic consistency, restore images efficiently. FlowIE [53] uses conditional rectified flow for faster inference with comparable restoration quality. However, diffusion models often suffer from poor identity consistency and loss of facial details in restored images. We find that randomness of diffusion models can be leveraged through reinforcement learning with composite reward mechanisms to generate higher-quality facial restorations.

RL in Vision Generation. Reinforcement learning has recently achieved remarkable success in improving large language model reasoning, particularly through policy gradient

approaches such as PPO [28] and GRPO [29]. In the text-to-image (T2I) generation field, many methods have explored incorporating policy gradient approaches (e.g., PPO) to align with human preferences. These methods explicitly cast diffusion denoising as a multi-step decision process and update the policy accordingly. DDPO [2] improves alignment and aesthetics by optimizing rewards tied to human feedback. DPOK [8] studies online RL with Kullback–Leibler (KL) regularization on SD [27]. As a complementary approach to RL, Diffusion-DPO [33] successfully adapts direct preference optimization to diffusion likelihoods, achieving significant improvements in human-preference alignment on SDXL [25]. Beyond standard diffusion models, Flow-GRPO [22] is the first to bring GRPO into flow-matching model. Building on this, TempFlow-GRPO [10] further improves efficiency and stability by introducing trajectory branching and enabling process-level rewards without an intermediate reward model. Motivated by these successes, we present the first integration of policy gradient-based online RL into the BFR domain.

3. preliminary

BFR Problem Modeling. BFR is an ill-posed inverse problem. From a mathematical perspective, given a low-quality observation c_{LQ} , the posterior distribution of its corresponding high-quality x_0 , denoted as $p(x_0|c_{LQ})$, has multiple feasible solutions [24]. This posterior can be modeled as a mixture distribution:

$$p(x_0|c_{LQ}) = \sum_{k=1}^K w_k \cdot p_k(x_0|c_{LQ}). \quad (1)$$

Here, K represents the number of possible high-quality solutions. Each distribution $p_k(x_0|c_{LQ})$ represents a real face distribution compatible with c_{LQ} , having a specific identity, expression, or detail, with a peak at μ_k . The w_k denotes the probability of the k -th solution, where $\sum w_k = 1$. This multi-solution nature poses a challenge for existing methods. Without dedicated exploration mechanisms, restoration models tend to converge toward average solutions, resulting in blurry faces with weakened textural detail [23].

DDIM. Diffusion models generate data through forward noise addition and reverse denoising processes. In the forward diffusion process, the data is progressively perturbed by Gaussian noise, defined as $q(x_t|x_{t-1}) = \mathcal{N}(\sqrt{\alpha_t}x_{t-1}, (1-\alpha_t)\mathbf{I})$, where $\alpha_t \in (0, 1]$ controls the noise intensity, and x_t represents the noisy data at time step t .

The denoising process recovers data via the conditional distribution $p_\theta(x_{t-1}|x_t, c)$, where c is a condition. In the DDIM [32] framework, the network predicts the noise $\epsilon_\theta(x_t, t, c)$. The one-step denoising formula (from t to $t-1$)

is given by:

$$\mu_\theta(x_t, t, c) = \sqrt{\alpha_{t-1}} \cdot \frac{x_t - \sqrt{1-\alpha_t} \cdot \epsilon_\theta(x_t, t, c)}{\sqrt{\alpha_t}} \quad (2)$$

$$+ \sqrt{1-\alpha_{t-1} - \sigma_t^2} \cdot \epsilon_\theta(x_t, t, c),$$

$$x_{t-1} = \mu_\theta(x_t, t, c) + \sigma_t \cdot \epsilon_t, \quad \epsilon_t \sim \mathcal{N}(\mathbf{0}, \mathbf{I}). \quad (3)$$

where $\sigma_t = \eta \sqrt{\frac{1-\alpha_{t-1}}{1-\alpha_t} \cdot \left(1 - \frac{\alpha_t}{\alpha_{t-1}}\right)}$, and $\eta \in [0, 1]$ controls the randomness. When $\eta = 0$, the sampling is deterministic, producing a fixed generation path. When $\eta > 0$, random noise ϵ is introduced, bringing randomness.

[8] proposes that DDIM can be formulated as a Markov Decision Process (MDP) defined by the tuple $(S, A, \rho_0, \pi, P, R)$. At time step t , the state is $s_t \triangleq (c, t, x_t)$. The action is the denoised sample predicted by the model, $a_t \triangleq x_{t-1}$, with the policy defined as $\pi(a_t|s_t) \triangleq \pi_\theta(x_{t-1}|x_t, c)$. The state transition is deterministic, given by $P(s_{t+1}|s_t, a_t) \triangleq (\delta_c, \delta_{a_t})$, where δ_c denotes the Dirac distribution at c . The initial state distribution is $P_0(s_0) \triangleq (p(c), \mathcal{N}(0, \mathbf{I}))$. The reward is provided only at the final step: $R(s_t, a_t) \triangleq r(x_0, c)$. When $\eta > 0$, the DDIM MDP can achieve reinforcement learning training.

4. Methodology

LRPO is an approach that enhances the BFR task using online RL, as shown in Figure 2. First, we initialize its policy network with an *off-the-shelf* diffusion-based face restoration model. Specifically, we employ DiffBIR [21] (our base model), a ControlNet-based [49] approach that uses the LQ input as a control signal to guide restoration. Based on the GRPO [29] algorithm, we propose three core innovations for the BFR task: (1) We design a composite reward function that provides rewards for the diffusion denoising process. (2) We propose a ground-truth guided likelihood regularization term to penalize policy updates that deviate from real face data. (3) We develop a noise-aware advantage assignment mechanism to appropriately weight advantages based on denoising step significance. LRPO is designed to post-train off-the-shelf face restoration models via RL, thereby extending their performance frontier. After training, the RL component is discarded, so no additional inference overhead is introduced to the base model.

4.1. Group Relative Policy Optimization

The optimization goal of reinforcement learning is to maximize the expected cumulative reward. Unlike PPO [28], GRPO [29] samples a group of G trajectories $\{\{x_T^{(i)}, x_{T-1}^{(i)}, \dots, x_0^{(i)}\}\}_{i=1}^G$, from the policy $\pi_{\theta_{\text{old}}}$, obtaining G candidate reconstructions $\hat{x}_0^{(i)}$, which are decoded from $x_0^{(i)}$ in latent diffusion, and their rewards $r^{(i)} =$

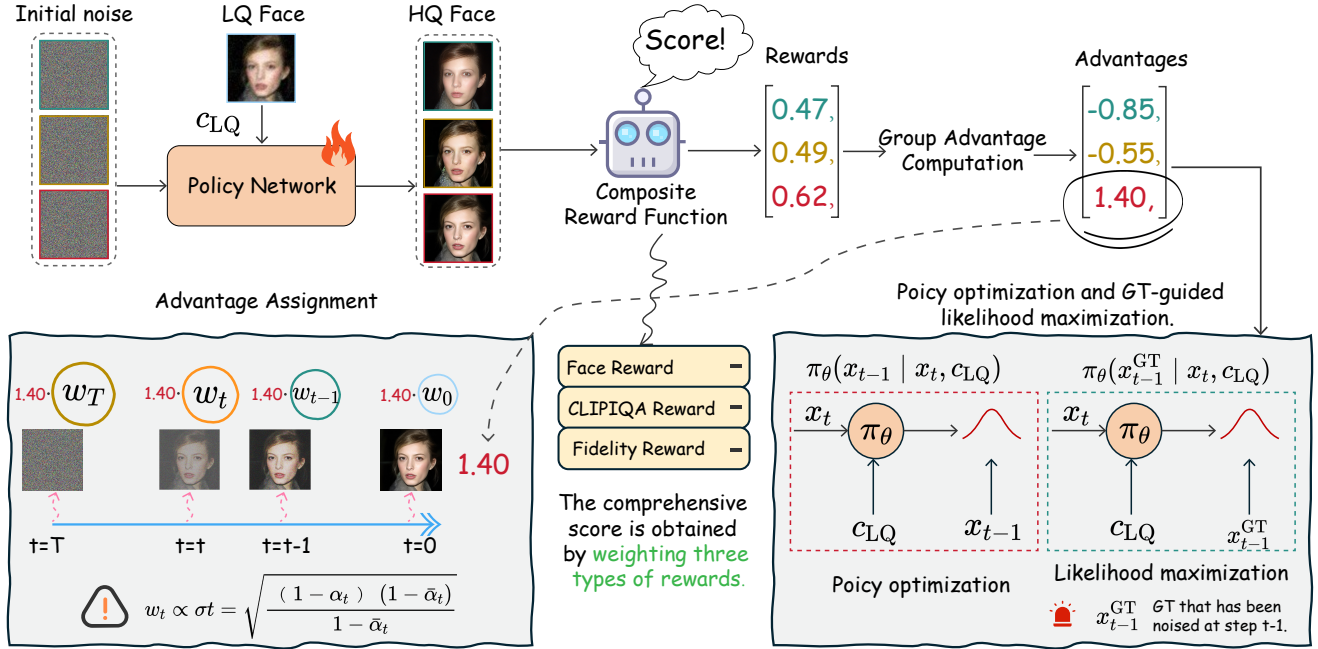


Figure 2. The overview of our proposed LRPO framework. The policy network produces multiple HQ restoration candidates from a single LQ input, which are then assessed by the reward function and transformed into advantage scores. The framework assigns weighted advantage scores to individual denoising steps according to their contribution to restoration quality, and integrates ground-truth guided likelihood regularization into the RL optimization objective to maintain fidelity.

$r(\hat{x}_0^{(i)}, x_{GT})$, where x_{GT} denotes the ground truth corresponding to $\hat{x}_0^{(i)}$. Then, the advantage of the i -th sampled trajectory at time t is calculated by normalizing the group-level rewards:

$$\hat{A}_t^{(i)} = \frac{r^{(i)} - \text{mean}(\{r^{(i)}\}_{i=1}^G)}{\text{std}(\{r^{(i)}\}_{i=1}^G)}. \quad (4)$$

Finally, the GRPO algorithm updates the policy model by maximizing the following objective:

$$\mathcal{J}_{\text{DDIM-GRPO}}(\theta) = \mathbb{E}_{c_{LQ}, \{\hat{x}^{(i)}\}_{i=1}^G} [\mathcal{L}(\theta)], \quad (5)$$

$$\mathcal{L}(\theta) = \frac{1}{G} \sum_{i=1}^G \frac{1}{T} \sum_{t=0}^{T-1} \left[\min \left(r_t^{(i)}(\theta) \hat{A}_t^{(i)}, \text{clip} \left(r_t^{(i)}(\theta), 1 - \epsilon, 1 + \epsilon \right) \hat{A}_t^{(i)} \right) - \beta D_{KL}(\pi_\theta \| \pi_{\text{ref}}) \right]. \quad (6)$$

where $r_t^{(i)}(\theta) = \frac{\pi_\theta(x_{t-1}^{(i)} | x_t^{(i)}, c_{LQ})}{\pi_{\theta_{\text{old}}}(x_{t-1}^{(i)} | x_t^{(i)}, c_{LQ})}$, with T denoting the total timesteps and π_{ref} denotes the initialized pretrained model.

Due to the inherent randomness of the Diffusion model, given the same LQ face c_{LQ} , a set of diverse candidate faces

$\{\hat{x}_0^{(1)}, \hat{x}_0^{(2)}, \dots, \hat{x}_0^{(G)}\}$ can be generated from policy π_θ . Ideally, when π_θ learns a posterior distribution capturing different potential solutions, the generated samples cluster around distinct peaks $\{\mu_k\}$ in the solution space. Such diverse candidates enable the optimization process to make meaningful comparisons and drive policy improvements.

Once obtaining the candidate set, we evaluate each generated sample $\hat{x}_0^{(i)}$ using the composite reward function $r(\cdot)$. The GRPO algorithm then transforms the absolute rewards $r^{(i)}$ into within-group relative advantages $\hat{A}_t^{(i)}$ (See Eq. 4), which improves the ability to distinguish between high and low-quality solutions while reducing sensitivity to reward scaling. The core insight of this transformation is to redirecting optimization from absolute quality assessment (“how good is this solution?”) to relative comparison (“how does this solution rank within the group?”). Consequently, the policy gradient update direction is proportional to:

$$\sum_{i=1}^G \sum_{t=0}^{T-1} \hat{A}_t^{(i)} \nabla_\theta \log \pi_\theta(a_t^{(i)} | s_t^{(i)}). \quad (7)$$

Thus, the following conclusion can be drawn: When a sample’s reward exceeds the group average, its advantage $\hat{A}_t^{(i)}$ is positive, increasing the policy’s selection probability; conversely, below-average rewards yield negative advantages

$\hat{A}_t^{(j)}$, reducing selection likelihood for suboptimal solutions. This group sampling approach enables parallel exploration of the policy’s learned solution space. To fully exploit GRPO’s ability to amplify good solutions while suppressing bad ones, we introduce three key innovations that improve exploration efficiency and enhance face restoration quality.

4.2. Likelihood-Regularized Policy Optimization

Composite Reward Function. To effectively guide the optimization of the policy network π_θ and enable it to find a better balance in the complex Perception-Distortion Trade-off [3], we design a multi-objective composite reward function, $R(\hat{\mathbf{x}}_0, \mathbf{x}_{\text{GT}})$. This composite function measures the quality of generated face images $\hat{\mathbf{x}}_0$ from three complementary perspectives:

- *Human Preference Reward* (r_{pref}): We employ a Face Reward Model [40], pre-trained on a human preference dataset, to score the overall realism and naturalness of facial details, ensuring alignment with human aesthetic preferences.
- *Perceptual Quality* (r_{aq}): We incorporate CLIP-IQA [34], a no-reference image quality assessment metric, to objectively measure perceptual quality using knowledge from pre-trained CLIP [26] models.
- *Fidelity Reward* (r_{fid}): We formulate a fidelity reward based on feature similarity and wavelet low-frequency constraints to enforce identity consistency, resulting in substantial fidelity improvements (see Appendix C for implementation details).

The final total reward $R(\cdot)$ is defined as the weighted sum of these three components:

$$R(\hat{\mathbf{x}}_0, \mathbf{x}_{\text{GT}}) = \lambda_1 r_{\text{pref}}(\hat{\mathbf{x}}_0) + \lambda_2 r_{\text{aq}}(\hat{\mathbf{x}}_0) + \lambda_3 r_{\text{fid}}(\hat{\mathbf{x}}_0, \mathbf{x}_{\text{GT}}). \quad (8)$$

where $\lambda_{(\cdot)}$ are the weight coefficients for each term.

Ground-truth Guided Likelihood Regularization. Optimization based solely on reward maximization is susceptible to reward hacking—the policy may exploit reward function biases to produce unrealistic outputs. We address this with ground-truth (GT) guided likelihood regularization $\mathcal{R}_{\text{likelihood}}$, activated only in the final S timesteps, to maintain realistic and natural face generation.

The regularization leverages GT supervision by using ideal denoising trajectories derived from $\hat{\mathbf{x}}^{\text{GT}}$. For each GT image, we pre-compute the ideal latent trajectory $\{\mathbf{x}^{\text{GT}}\}_{t=0}^T$ through forward noising. During training, when the policy π_θ samples a state \mathbf{x}_t , we apply regularization by maximizing the log-likelihood of the model producing the ideal subsequent state $\mathbf{x}_{t-1}^{\text{GT}}$. Thus, the regularization item is defined as:

$$\mathcal{R}_{\text{likelihood}} = -\log \pi_\theta(\mathbf{x}_{t-1}^{\text{GT}} | \mathbf{x}_t, \mathbf{c}_{\text{LQ}}), \quad (9)$$

$$\mathcal{R}_{\text{likelihood}} \propto \frac{\|\mathbf{x}_{t-1}^{\text{GT}} - \mu_\theta(\mathbf{x}_t, t, \mathbf{c}_{\text{LQ}})\|_2^2}{2\sigma_t^2}. \quad (10)$$

Where μ_θ and σ_t refer to the mean and standard deviation of DDIM’s one-step denoising, with the detailed form provided in Sec. 3. As shown in Eq. 9, this loss term encourages the policy network π_θ to predict a high-probability distribution centered around the ideal target $\mathbf{x}_{t-1}^{\text{GT}}$ at its explored state \mathbf{x}_t . This is equivalent to minimizing the variance-weighted Euclidean distance between the predicted mean $\mu_\theta(\mathbf{x}_t, t, \mathbf{c})$ and the ideal state $\mathbf{x}_{t-1}^{\text{GT}}$. The likelihood regularization $\mathcal{R}_{\text{likelihood}}$ maintains alignment between restored image and authentic facial distributions, substituting for the standard KL divergence term in GRPO.

Noise-Level Advantage Assignment. Conventional GRPO-based approaches [8, 22] treat all timesteps equally when assigning advantage weights, ignoring the inherently non-uniform importance of different steps in the diffusion process. To address this, inspired by previous work [10], we introduce a noise-level-aware advantage assignment approach that correlates advantage weights with the exploration magnitude achieved at each denoising step. In DDIM sampling, the single-step exploration radius from \mathbf{x}_t to \mathbf{x}_{t-1} is determined by the standard deviation σ_t of the added noise. Therefore, we set the timestep weight w_t proportional to σ_t :

$$w_t \propto \sigma_t, \quad \text{s.t.} \quad \frac{1}{T} \sum_{t=0}^{T-1} w_t = 1. \quad (11)$$

The specific form of σ_t is detailed in Sec. 3. After normalizing the weights $\{w_t\}_{t=1}^T$, we apply them to weight the original advantage $\hat{A}_t^{(i)}$, yielding the final advantage $\tilde{A}_t^{(i)}$ for policy update:

$$\tilde{A}_t^{(i)} = w_t \cdot \hat{A}_t^{(i)}. \quad (12)$$

Since σ_t decreases from high initial values to nearly zero, early denoising steps possess greater exploration capability. By weighting these steps more heavily in advantage computation, we facilitate enhanced exploration that yields more diverse high-quality restoration outcomes. Simultaneously, it reduces interference during the high-frequency detail refinement that occurs in later denoising phases. This allocation strategy effectively performs weighted adjustment of policy gradients, as detailed in Appendix A.

LRPO Optimization Objective. By combining these strategies, we formulate an optimization objective that maximizes policy return while applying likelihood regularization to prevent unrealistic restorations:

$$\mathcal{J}_{\text{LRPO}}(\theta) = \mathbb{E}_{\mathbf{c}_{\text{LQ}}, \{\hat{\mathbf{x}}^{(i)}\}_{i=1}^G} [\mathcal{L}_{\text{LRPO}}(\theta)], \quad (13)$$

$$\mathcal{L}_{\text{LRPO}}(\theta) = \frac{1}{G} \sum_{i=1}^G \frac{1}{T} \sum_{t=0}^{T-1} \left[\min \left(r_t^{(i)}(\theta) \hat{A}_t^{(i)}, \right. \right. \\ \left. \left. \text{clip} \left(r_t^{(i)}(\theta), 1 - \epsilon, 1 + \epsilon \right) \hat{A}_t^{(i)} \right) + \alpha \mathcal{R}_{\text{likelihood}}^{(i)} \right]. \quad (14)$$

Compared to Eq. 5, we replace the KL divergence component with GT-guided likelihood regularization in our optimization objective.

5. Experiments

5.1. Experimental Settings

Experimental hyperparameters are detailed in Appendix B, and composite reward function configurations are provided in Appendix C.

Training and Testing Data. We use face images from the FFHQ [16] dataset for training. The degradation strategy from HQ to LQ is based on the following degradation function: $\mathbf{I}_{LQ} = \left\{ \left[(\mathbf{I}_{HQ} \otimes \mathbf{k}_\sigma) \downarrow_r + \mathbf{n}_\delta \right]_{\text{JPEG}_q} \right\}_{\uparrow_r}$, where the HQ images are first convolved with a Gaussian kernel \mathbf{k}_σ , followed by a downsampling with a factor of r , and then corrupted with Gaussian noise \mathbf{n}_δ . Subsequently, the images undergo JPEG compression with a quality factor of q . Finally, the LQ image is resized back to the original 512×512 . Here, σ , r , δ , and q are randomly sampled from the intervals $[0.1, 12]$, $[1, 12]$, $[0, 15]$, and $[30, 100]$, respectively. Follow previous work Gu et al. [9], Wang et al. [36], we employ the synthetic dataset CelebA-Test [13] and two real-world datasets [36] (*i.e.*, LFW-Test and WebPhoto-Test) to validate our method.

Evaluation Metrics. On the CelebA-Test dataset, we utilized six common reference-based metrics: SSIM [37], PSNR, LPIPS [50], CLIP Score [11], Deg. [36], and LMD [9], where Deg. and LMD are identity consistency metrics, along with four non-reference metrics: MUSIQ [17], MANIQA [43], CLIPQA [34], and Aesthetic [19].

Comparison Methods. We compare with not only the base models but also the latest state-of-the-art methods, including GFGAN [4], CodeFormer [52], VQFR [9], DR2+SPAR [39], RestoreFormer [38], DiffFace [48], OSediff [41], DiffBIR [21], FlowIE [53] and InterLCM [20]. Among them, FlowIE and InterLCM use ODE solvers.

5.2. Main Results

Results on Synthetic Data. As shown in Table 1, LRPO achieves improvements on all metrics compared with DiffBIR on the synthetic CelebA-Test dataset. These results indicate that our RL framework simultaneously improves perceptual quality and identity preservation in restored faces. Furthermore, LRPO achieves superior performance compared to state-of-the-art approaches across the majority of evaluation metrics, including SSIM, LMD, and MUSIQ, confirming that it enhances identity consistency while maintaining perceptual quality. Figure 3 demonstrates LRPO’s superior performance over methods that fail to restore faces. LRPO delivers more realistic textures than the baseline, better identity alignment than OSediff, and more natural results

without the over-smoothing seen in OSediff and DiffBIR. Appendix F contains the complete qualitative results.

Results on Real-world Data. Table 2 shows the quantitative performance evaluation on real-world datasets LFW-Test and WebPhoto-Test. LRPO demonstrates significant performance gains compared to the base DiffBIR and outperforms other state-of-the-art approaches on MUSIQ and CLIP-IQA metrics. Qualitative results are illustrated in Figure 4. Due to severe degradation in real-world inputs, many approaches fail to restore texture details. In contrast, our method recovers more details while introducing fewer artifacts.

Human Preference Evaluation. A user study was conducted with 12 participants of varying backgrounds to evaluate 100 face images from the CelebA-Test dataset. Participants evaluated our method against the base model (DiffBIR) on two criteria: *fidelity* (identity preservation) and *realism* (naturalness with minimal artifacts). As shown in Table 3, our method outperforms the base model in both fidelity and realism according to human preferences.

5.3. Ablation Study

We conduct the ablation study on CelebA-Test dataset. As shown in Table 4, we analyze the effects of four key components: Reinforcement Learning (RL), Kullback-Leibler divergence (KL), GT guided likelihood regularization (Reg.), and noise-level advantage assignment (AdA). Variant 1 demonstrates improvements across all metrics after incorporating RL, confirming that RL directly enhances BFR performance. However, adding KL divergence in Variant 2 degrades all metrics without improving visual quality (See Figure 5(a)). We therefore remove KL divergence from the RL objective in Eq. 13, reducing computational cost while maintaining visual quality. Without AdA (Variant 3), the model suffers from detail blurring caused by over-optimization during late denoising stages (Figure 5(b)). Removing Reg. (Variant 4) leads to decreased SSIM scores and poor fidelity, with the model producing unrealistic, fantasy-like textures as shown in Figure 5(c). Training dynamics show that our noise-level advantage assignment facilitates faster convergence to high-reward restoration trajectories, while GT guided likelihood regularization enhances the consistency with the true distribution. (Appendix D).

In addition, Figure 6 shows the experiments conducted to select the number of trajectories G within each group. Because $G = 9$ exhibits superior performance in terms of both structural similarity and identity consistency, we set $G = 9$ for the training stage. The proposed likelihood regularizer is applied only during the last S denoising steps. Throughout training, varying S leads to different reward curves, as shown in Figure 7. Choosing an excessively large S introduces overly strong penalties that conflict with the RL learning trajectory, ultimately causing training collapse. $S = 5$ achieves convergence to a higher reward score without

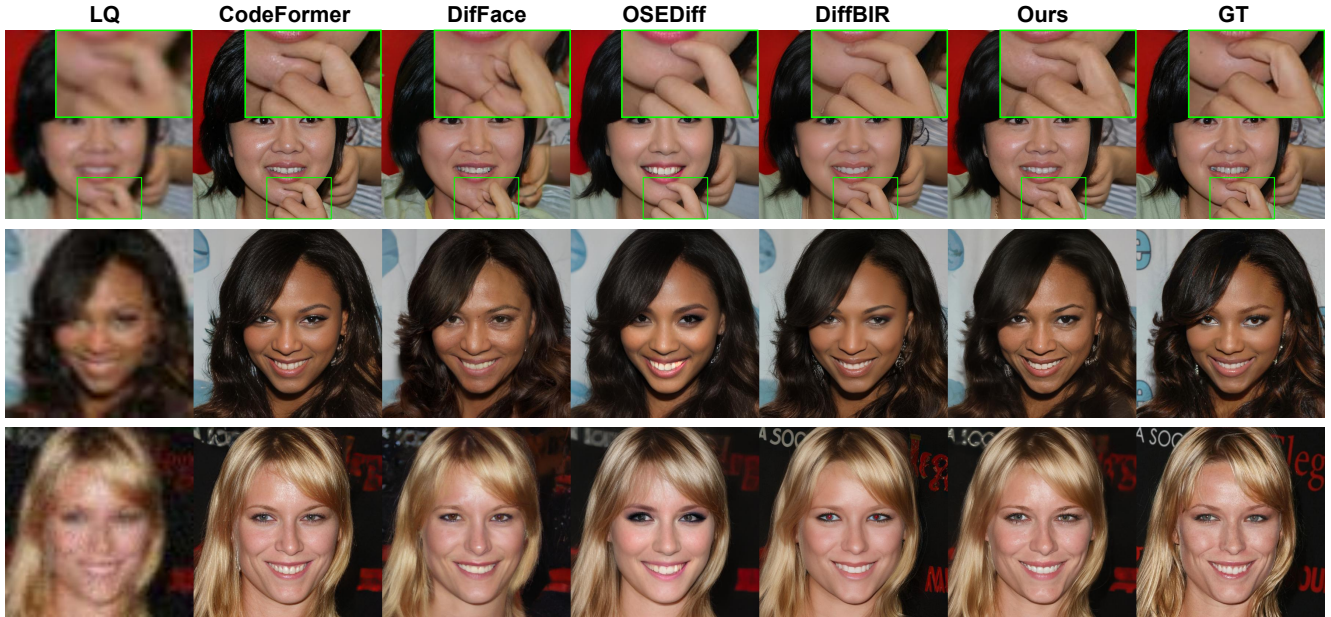


Figure 3. Qualitative results on CelebA-Test datasets. (Zoom in for details)

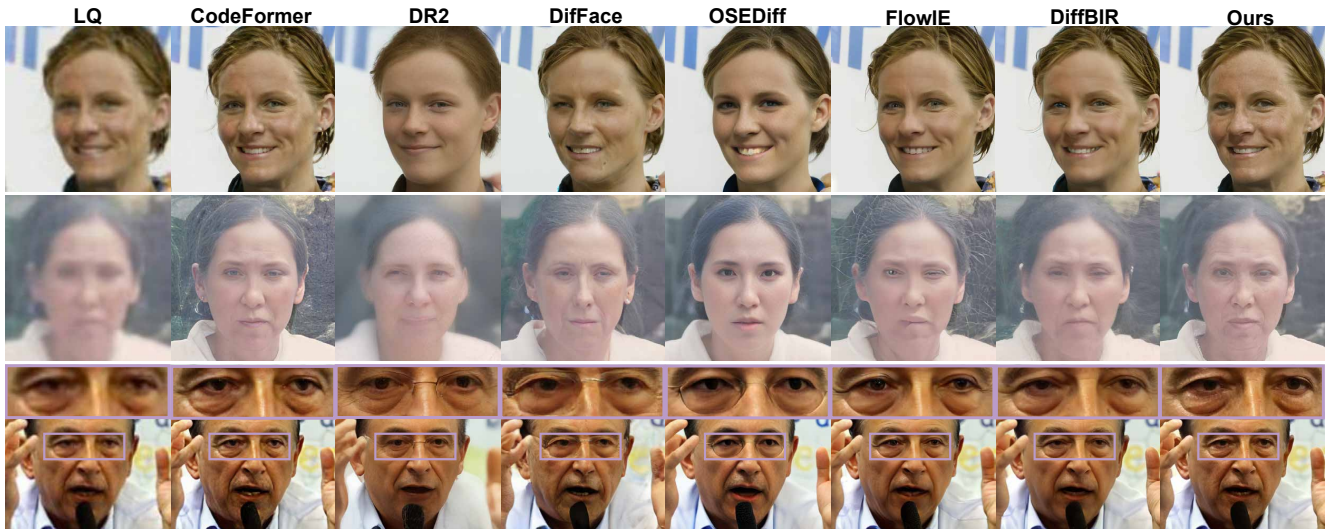


Figure 4. Qualitative results on real-world datasets. (Zoom in for details)

causing training collapse; therefore, we adopt $S = 5$.

6. conclusion

In this work, we propose LRPO, the first online reinforcement learning framework applied to BFR tasks. LRPO exploits RL’s inherent exploration mechanisms to overcome the limitations of deterministic restoration methods, simultaneously improving perceptual quality and identity preservation. LRPO integrates three critical innovations: a composite reward function for multi-perspective image evaluation, GT guided likelihood regularization for fidelity preservation, and noise-level advantage assignment for efficient optimization.

Comprehensive experiments validate LRPO’s effectiveness in enhancing both identity consistency and perceptual quality compared to existing approaches.

References

- [1] Dario Amodei, Chris Olah, Jacob Steinhardt, Paul Christiano, John Schulman, and Dan Mané. Concrete problems in ai safety. *arXiv preprint arXiv:1606.06565*, 2016. 2
- [2] Kevin Black, Michael Janner, Yilun Du, Ilya Kostrikov, and Sergey Levine. Training diffusion models with reinforcement learning. *arXiv preprint arXiv:2305.13301*, 2023. 3
- [3] Yochai Blau and Tomer Michaeli. The perception-distortion

Table 1. Performance comparisons on CelebA-Test. The highest score for each metric is highlighted in red, the second-highest in blue. Metrics with \uparrow indicate higher is better, \downarrow means lower is better. Values in parentheses represent our method’s improvements over the base DiffBIR model.

Methods	SSIM \uparrow	PSNR \uparrow	LPIPS \downarrow	CLIP Score \uparrow	Deg. \downarrow	LMD \downarrow	MUSIQ \uparrow	MANIQA \uparrow	Aesthetic \uparrow	CLIPQA \uparrow
Input	0.6994	25.33	0.4866	0.7894	47.94	3.7560	17.00	0.3957	4.0484	0.2957
GFP-GAN	0.6772	24.65	0.3646	0.8410	34.58	2.4110	73.90	0.6522	5.6992	0.6781
CodeFormer	0.6925	25.85	0.3335	0.8931	31.08	1.9963	74.23	0.6520	5.8103	0.6493
VQFR	0.6654	23.76	0.3557	0.8562	42.48	2.9444	73.84	0.6544	5.7844	0.6750
DR2+SPAR	0.6512	22.89	0.4146	0.7437	57.24	4.5449	70.19	0.6374	5.6602	0.5960
DiffFace	0.6762	24.80	0.3994	0.8380	45.81	2.9766	68.96	0.6204	5.4708	0.5711
OSDiff	0.6864	23.96	0.3478	0.7962	46.20	2.8871	73.41	0.6560	5.7720	0.6120
FlowIE	0.6769	24.85	0.3442	0.8961	33.44	2.1995	74.08	0.6720	5.6782	0.6866
InterLCM	0.6819	24.88	0.3349	0.8905	33.58	2.1519	75.16	0.6781	5.7735	0.6748
DiffBIR	0.6775	25.44	0.3811	0.8877	35.16	2.2661	74.46	0.6752	5.7943	0.7200
LRPO (ours)	0.7021	26.15	0.3635	0.9100	31.19	1.9533	75.24	0.6808	5.8126	0.8061
	(+0.0246)	(+0.71)	(+0.0176)	(+0.0223)	(+3.97)	(+0.3128)	(+0.78)	(+0.0056)	(+0.0183)	(+0.0861)

Table 2. Performance comparisons on wild datasets. The highest score is highlighted in red, and the second-highest in blue. Metrics with \uparrow indicate higher is better.

Dataset Methods	LFW-Test		WebPhoto-Test	
	MUSIQ \uparrow	CLIPQA \uparrow	MUSIQ \uparrow	CLIPQA \uparrow
Input	26.87	0.2834	18.63	0.4128
GFP-GAN	73.57	0.6983	72.09	0.6888
CodeFormer	70.69	0.6335	71.16	0.6573
VQFR	74.39	0.7100	70.91	0.6767
DR2+SPAR	72.22	0.6427	63.65	0.5586
DiffFace	69.85	0.6110	65.21	0.5821
OSDiff	73.40	0.6327	72.60	0.6454
FlowIE	64.29	0.5974	71.45	0.6838
InterLCM	74.18	0.6588	73.91	0.6658
DiffBIR	73.71	0.7296	67.45	0.6630
LRPO (ours)	74.60	0.8073	72.71	0.7040
	(+0.89)	(+0.0777)	(+5.26)	(+0.0410)

Table 3. User study. Participants selected the winner between DiffBIR and LRPO restored images in terms of fidelity and realism.

Comparison	Fidelity %	Realism %
DiffBIR vs LRPO	38.1% vs 61.9%	27.6% vs 72.4%

Table 4. Ablation Study of LRPO

Struct	RL	KL	Reg	AdA	SSIM \uparrow	LMD \downarrow	CLIPQA \uparrow
Base					0.6775	2.2661	0.7200
Variant 1	✓				0.6849	2.0503	0.7809
Variant 2	✓	✓			0.6750	2.1602	0.7816
Variant 3	✓		✓		0.6867	2.0078	0.7852
Variant 4	✓			✓	0.6806	1.9551	0.7980
LRPO	✓		✓	✓	0.7021	1.9533	0.8061

tradeoff. In *Proceedings of the IEEE conference on computer vision and pattern recognition*, pages 6228–6237, 2018. 5

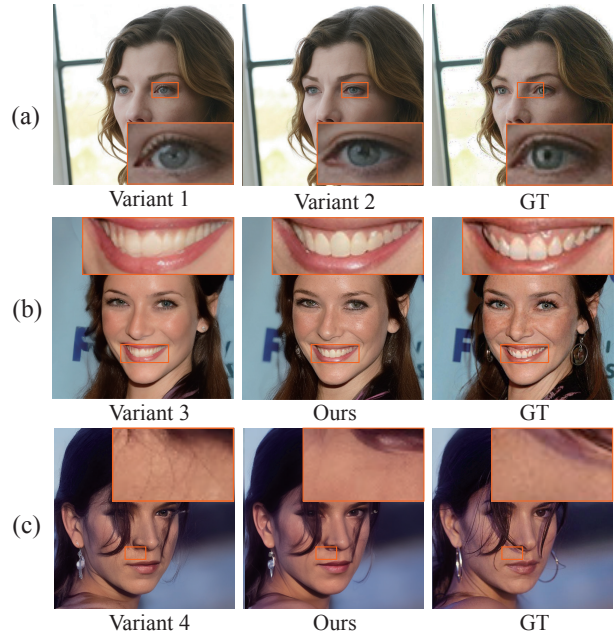


Figure 5. Ablation study visualizations.

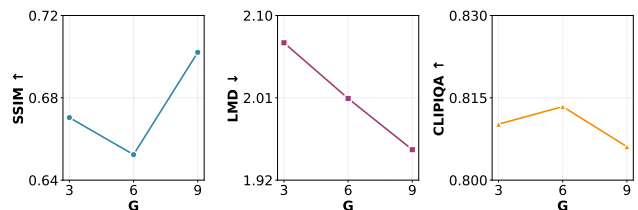


Figure 6. Quantitative metrics under different group sizes G .

[4] Kelvin CK Chan, Xintao Wang, Xiangyu Xu, Jinwei Gu, and Chen Change Loy. Glean: Generative latent bank for large-factor image super-resolution. In *Proceedings of*

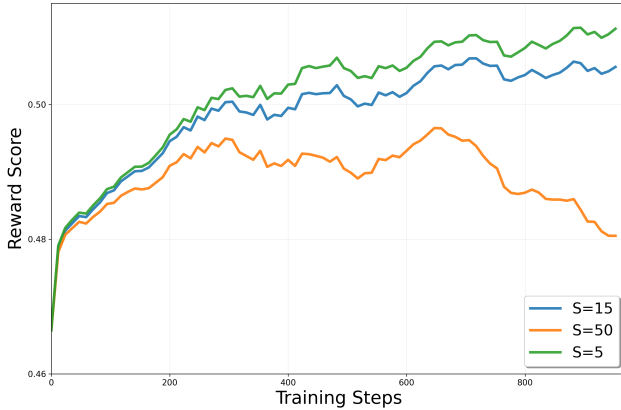


Figure 7. Reward curves of different S values within the likelihood regularization term

the *IEEE/CVF Conference on Computer Vision and Pattern Recognition (CVPR)*, 2021. 1, 6

- [5] Chaofeng Chen, Xiaoming Li, Lingbo Yang, Xianhui Lin, Lei Zhang, and Kwan-Yee K Wong. Progressive semantic-aware style transformation for blind face restoration. In *Proceedings of the IEEE/CVF Conference on Computer Vision and Pattern Recognition (CVPR)*, 2021. 1
- [6] Xiaoxu Chen, Jingfan Tan, Tao Wang, Kaihao Zhang, Wenhao Luo, and Xiaochun Cao. Towards real-world blind face restoration with generative diffusion prior. *IEEE Transactions on Circuits and Systems for Video Technology*, 2024. 1
- [7] Yu Chen, Ying Tai, Xiaoming Liu, Chunhua Shen, and Jian Yang. Fsrnet: End-to-end learning face super-resolution with facial priors. In *Proceedings of the IEEE/CVF Conference on Computer Vision and Pattern Recognition (CVPR)*, 2018. 1
- [8] Ying Fan, Olivia Watkins, Yuqing Du, Hao Liu, Moonkyung Ryu, Craig Boutilier, Pieter Abbeel, Mohammad Ghavamzadeh, Kangwook Lee, and Kimin Lee. Dpokr: Reinforcement learning for fine-tuning text-to-image diffusion models. *Advances in Neural Information Processing Systems*, 36:79858–79885, 2023. 1, 3, 5
- [9] Yuchao Gu, Xintao Wang, Liangbin Xie, Chao Dong, Gen Li, Ying Shan, and Ming-Ming Cheng. Vqfr: Blind face restoration with vector-quantized dictionary and parallel decoder. In *European Conference on Computer Vision (ECCV)*, 2022. 1, 6
- [10] Xiaoxuan He, Siming Fu, Yuke Zhao, Wanli Li, Jian Yang, Dacheng Yin, Fengyun Rao, and Bo Zhang. Tempflow-grpo: When timing matters for grpo in flow models. *arXiv preprint arXiv:2508.04324*, 2025. 3, 5
- [11] Jack Hessel, Ari Holtzman, Maxwell Forbes, and Yejin Choi. Clipscore: A reference-free evaluation metric for image captioning. *arXiv preprint arXiv:2104.08718*, 2021. 6
- [12] Jonathan Ho, Ajay Jain, and Pieter Abbeel. Denoising diffusion probabilistic models. *Advances in Neural Information Processing Systems (NeurIPS)*, 2020. 2
- [13] Tero Karras, Timo Aila, Samuli Laine, and Jaakko Lehtinen. Progressive growing of gans for improved quality, stability, and variation. *arXiv preprint arXiv:1710.10196*, 2017. 6
- [14] Tero Karras, Samuli Laine, and Timo Aila. A style-based generator architecture for generative adversarial networks. In *Proceedings of the IEEE/CVF Conference on Computer Vision and Pattern Recognition (CVPR)*, 2019. 1
- [15] Tero Karras, Samuli Laine, Miika Aittala, Janne Hellsten, Jaakko Lehtinen, and Timo Aila. Analyzing and improving the image quality of stylegan. In *Proceedings of the IEEE/CVF Conference on Computer Vision and Pattern Recognition (CVPR)*, 2020. 1
- [16] T. Karras, S. Laine, and T. Aila. A style-based generator architecture for generative adversarial networks. *IEEE Transactions on Pattern Analysis Machine Intelligence*, 43(12): 4217–4228, 2021. 6
- [17] Junjie Ke, Qifei Wang, Yilin Wang, Peyman Milanfar, and Feng Yang. Musiq: Multi-scale image quality transformer. In *Proceedings of the IEEE/CVF International Conference on Computer Vision (ICCV)*, 2021. 6
- [18] Deokyun Kim, Minseon Kim, Gihyun Kwon, and Dae-Shik Kim. Progressive face super-resolution via attention to facial landmark. *arXiv preprint arXiv:1908.08239*, 2019. 1
- [19] LAION-AI. Aesthetic predictor: A linear estimator on top of clip to predict the aesthetic quality of pictures. <https://github.com/LAION-AI/aesthetic-predictor>, 2022. Accessed: 2025-05-13. 6
- [20] Senmao Li, Kai Wang, Joost van de Weijer, Fahad Shahbaz Khan, Chun-Le Guo, Shiqi Yang, Yaxing Wang, Jian Yang, and Ming-Ming Cheng. Interlcm: Low-quality images as intermediate states of latent consistency models for effective blind face restoration. *arXiv preprint arXiv:2502.02215*, 2025. 2, 6
- [21] Xinqi Lin, Jingwen He, Ziyang Chen, Zhaoyang Lyu, Bo Dai, Fanghua Yu, Yu Qiao, Wanli Ouyang, and Chao Dong. Diffbir: Toward blind image restoration with generative diffusion prior. In *European Conference on Computer Vision (ECCV)*, 2024. 1, 2, 3, 6
- [22] Jie Liu, Gongye Liu, Jiajun Liang, Yangguang Li, Jiaheng Liu, Xintao Wang, Pengfei Wan, Di Zhang, and Wanli Ouyang. Flow-grpo: Training flow matching models via online rl. *arXiv preprint arXiv:2505.05470*, 2025. 1, 3, 5
- [23] Andreas Lugmayr, Martin Danelljan, Luc Van Gool, and Radu Timofte. Srflo: Learning the super-resolution space with normalizing flow. In *European conference on computer vision*, pages 715–732. Springer, 2020. 3
- [24] Sachit Menon, Alexandru Damian, Shijia Hu, Nikhil Ravi, and Cynthia Rudin. Pulse: Self-supervised photo upsampling via latent space exploration of generative models. In *Proceedings of the IEEE/CVF Conference on Computer Vision and Pattern Recognition (CVPR)*, 2020. 3
- [25] Dustin Podell, Zion English, Kyle Lacey, Andreas Blattmann, Tim Dockhorn, Jonas Müller, Joe Penna, and Robin Rombach. Sdxl: Improving latent diffusion models for high-resolution image synthesis. *arXiv preprint arXiv:2307.01952*, 2023. 3
- [26] Alec Radford, Jong Wook Kim, Chris Hallacy, Aditya Ramesh, Gabriel Goh, Sandhini Agarwal, Girish Sastry, Amanda Askell, Pamela Mishkin, Jack Clark, et al. Learning transferable visual models from natural language supervision. In *International Conference on Machine Learning (ICML)*, 2021. 5

- [27] Robin Rombach, Andreas Blattmann, Dominik Lorenz, Patrick Esser, and Björn Ommer. High-resolution image synthesis with latent diffusion models. In *Proceedings of the IEEE/CVF Conference on Computer Vision and Pattern Recognition (CVPR)*, 2022. 2, 3
- [28] John Schulman, Filip Wolski, Prafulla Dhariwal, Alec Radford, and Oleg Klimov. Proximal policy optimization algorithms. *arXiv preprint arXiv:1707.06347*, 2017. 3
- [29] Zhihong Shao, Peiyi Wang, Qihao Zhu, Runxin Xu, Junxiao Song, Xiao Bi, Haowei Zhang, Mingchuan Zhang, YK Li, Yang Wu, et al. Deepseekmath: Pushing the limits of mathematical reasoning in open language models. *arXiv preprint arXiv:2402.03300*, 2024. 1, 3
- [30] Joar Skalse, Nikolaus Howe, Dmitrii Krasheninnikov, and David Krueger. Defining and characterizing reward gaming. *Advances in Neural Information Processing Systems*, 35:9460–9471, 2022. 2
- [31] Jascha Sohl-Dickstein, Eric Weiss, Niru Maheswaranathan, and Surya Ganguli. Deep unsupervised learning using nonequilibrium thermodynamics. In *International Conference on Machine Learning (ICML)*, 2015. 2
- [32] Jiaming Song, Chenlin Meng, and Stefano Ermon. Denoising diffusion implicit models. *arXiv preprint arXiv:2010.02502*, 2020. 3
- [33] Bram Wallace, Meihua Dang, Rafael Rafailov, Linqi Zhou, Aaron Lou, Senthil Purushwalkam, Stefano Ermon, Caiming Xiong, Shafiq Joty, and Nikhil Naik. Diffusion model alignment using direct preference optimization. In *Proceedings of the IEEE/CVF Conference on Computer Vision and Pattern Recognition (CVPR)*, 2024. 3
- [34] Jianyi Wang, Kelvin CK Chan, and Chen Change Loy. Exploring clip for assessing the look and feel of images. In *Proceedings of the AAAI Conference on Artificial Intelligence (AAAI)*, 2023. 5, 6, 14
- [35] Junke Wang, Zhi Tian, Xun Wang, Xinyu Zhang, Weilin Huang, Zuxuan Wu, and Yu-Gang Jiang. Simplear: Pushing the frontier of autoregressive visual generation through pre-training, sft, and rl. *arXiv preprint arXiv:2504.11455*, 2025. 1
- [36] Xintao Wang, Yu Li, Honglun Zhang, and Ying Shan. Towards real-world blind face restoration with generative facial prior. In *Proceedings of the IEEE/CVF Conference on Computer Vision and Pattern Recognition (CVPR)*, 2021. 1, 6
- [37] Zhou Wang, Alan C Bovik, Hamid R Sheikh, and Eero P Simoncelli. Image quality assessment: from error visibility to structural similarity. *IEEE Transactions on Image Processing (TIP)*, 13(4):600–612, 2004. 6
- [38] Zhouxia Wang, Jiawei Zhang, Runjian Chen, Wenping Wang, and Ping Luo. Restoreformer: High-quality blind face restoration from undegraded key-value pairs. 2022. 6
- [39] Zhixin Wang, Ziyang Zhang, Xiaoyun Zhang, Huangjie Zheng, Mingyuan Zhou, Ya Zhang, and Yanfeng Wang. Dr2: Diffusion-based robust degradation remover for blind face restoration. In *Proceedings of the IEEE/CVF Conference on Computer Vision and Pattern Recognition (CVPR)*, 2023. 1, 2, 6
- [40] Bin Wu, Wei Wang, Yahui Liu, Zixiang Li, and Yao Zhao. Diffusionreward: Enhancing blind face restoration through reward feedback learning. *arXiv preprint arXiv:2505.17910*, 2025. 5, 13
- [41] Rongyuan Wu, Lingchen Sun, Zhiyuan Ma, and Lei Zhang. One-step effective diffusion network for real-world image super-resolution. *Advances in Neural Information Processing Systems (NeurIPS)*, 2024. 1, 6
- [42] Zeyue Xue, Jie Wu, Yu Gao, Fangyuan Kong, Lingting Zhu, Mengzhao Chen, Zhiheng Liu, Wei Liu, Qiushan Guo, Weilin Huang, et al. Dancegrp: Unleashing grp on visual generation. *arXiv preprint arXiv:2505.07818*, 2025. 1
- [43] Sidi Yang, Tianhe Wu, Shuwei Shi, Shanshan Lao, Yuan Gong, Mingdeng Cao, Jiahao Wang, and Yujiu Yang. Maniq: Multi-dimension attention network for no-reference image quality assessment. In *Proceedings of the IEEE/CVF Conference on Computer Vision and Pattern Recognition (CVPR)*, 2022. 6
- [44] Tao Yang, Peiran Ren, Xuansong Xie, and Lei Zhang. Gan prior embedded network for blind face restoration in the wild. In *Proceedings of the IEEE/CVF conference on Computer Vision and Pattern Recognition (CVPR)*, 2021. 1
- [45] Qiyang Yu, Zheng Zhang, Ruofei Zhu, Yufeng Yuan, Xiaochen Zuo, Yu Yue, Weinan Dai, Tiantian Fan, Gaohong Liu, Lingjun Liu, et al. Dapo: An open-source llm reinforcement learning system at scale. *arXiv preprint arXiv:2503.14476*, 2025. 1
- [46] Xin Yu, Basura Fernando, Bernard Ghanem, Fatih Porikli, and Richard Hartley. Face super-resolution guided by facial component heatmaps. In *European conference on computer vision (ECCV)*, 2018. 1
- [47] Shihao Yuan, Yahui Liu, Yang Yue, Jingyuan Zhang, Wangmeng Zuo, Qi Wang, Fuzheng Zhang, and Guorui Zhou. Ar-grpo: Training autoregressive image generation models via reinforcement learning. *arXiv preprint arXiv:2508.06924*, 2025. 1
- [48] Zongsheng Yue and Chen Change Loy. Difface: Blind face restoration with diffused error contraction. *IEEE Transactions on Pattern Analysis and Machine Intelligence (TPAMI)*, 2024. 1, 2, 6
- [49] Lvmin Zhang, Anyi Rao, and Maneesh Agrawala. Adding conditional control to text-to-image diffusion models. In *Proceedings of the IEEE/CVF International Conference on Computer Vision (ICCV)*, 2023. 3
- [50] Richard Zhang, Phillip Isola, Alexei A Efros, Eli Shechtman, and Oliver Wang. The unreasonable effectiveness of deep features as a perceptual metric. In *Proceedings of the IEEE/CVF Conference on Computer Vision and Pattern Recognition (CVPR)*, 2018. 6, 14
- [51] Hangqi Zhou, Chao Huang, Shangqi Gao, and Xiahai Zhuang. Vspsr: Explorable super-resolution via variational sparse representation. In *Proceedings of the IEEE/CVF Conference on Computer Vision and Pattern Recognition (CVPR)*, 2021. 1
- [52] Shangchen Zhou, Kelvin Chan, Chongyi Li, and Chen Change Loy. Towards robust blind face restoration with codebook lookup transformer. *Advances in Neural Information Processing Systems (NeurIPS)*, 2022. 1, 6
- [53] Yixuan Zhu, Wenliang Zhao, Ao Li, Yansong Tang, Jie Zhou, and Jiwen Lu. Flowie: Efficient image enhancement via

rectified flow. In *Proceedings of the IEEE/CVF Conference on Computer Vision and Pattern Recognition (CVPR), 2024*.
[2, 6](#)

Supplementary Material

Enhancing Blind Face Restoration through Online Reinforcement Learning

A. Advantage Weight as a Direct Gradient Coefficient

For a generative process parameterized by θ , the policy gradient in the DDIM optimization objective can be expressed as follows:

$$\nabla_{\theta} \mathcal{J}_{\text{LRPO}}(\theta) = \sum_{t=0}^{T-1} \mathbb{E}_{\mathbf{x}_T, \epsilon} \left[\nabla_{\theta} \log \pi_{\theta}(\mathbf{x}_{t-1} | \mathbf{x}_t, \mathbf{c}) (w_t \cdot \hat{A}_t) \right] \quad (15)$$

The core of the proof is to expand the log-policy gradient term, $\nabla_{\theta} \log \pi_{\theta}$. The log-policy is defined by the Gaussian sampling step:

$$\log \pi_{\theta}(\mathbf{x}_{t-1} | \mathbf{x}_t, \mathbf{c}) = -\frac{\|\mathbf{x}_{t-1} - \mu_{\theta}(\mathbf{x}_t, t, \mathbf{c})\|_2^2}{2\sigma_t^2} + \mathcal{C}_t \quad (16)$$

Taking the gradient with respect to θ :

$$\nabla_{\theta} \log \pi_{\theta}(\mathbf{x}_{t-1} | \mathbf{x}_t, \mathbf{c}) = \nabla_{\theta} \left(-\frac{\|\mathbf{x}_{t-1} - \mu_{\theta}(\mathbf{x}_t, t, \mathbf{c})\|_2^2}{2\sigma_t^2} \right) \quad (17)$$

$$= -\frac{1}{2\sigma_t^2} \cdot 2(\mathbf{x}_{t-1} - \mu_{\theta}(\mathbf{x}_t, t, \mathbf{c})) \cdot (-\nabla_{\theta} \mu_{\theta}(\mathbf{x}_t, t, \mathbf{c})) \quad (18)$$

$$= \frac{\mathbf{x}_{t-1} - \mu_{\theta}(\mathbf{x}_t, t, \mathbf{c})}{\sigma_t^2} \cdot \nabla_{\theta} \mu_{\theta}(\mathbf{x}_t, t, \mathbf{c}) \quad (19)$$

Since $\mathbf{x}_{t-1} = \mu_{\theta}(\mathbf{x}_t, t, \mathbf{c}) + \sigma_t \epsilon$ where $\epsilon \sim \mathcal{N}(\mathbf{0}, \mathbf{I})$:

$$\nabla_{\theta} \log \pi_{\theta}(\mathbf{x}_{t-1} | \mathbf{x}_t, \mathbf{c}) = \frac{\sigma_t \epsilon}{\sigma_t^2} \cdot \nabla_{\theta} \mu_{\theta}(\mathbf{x}_t, t, \mathbf{c}) = \frac{\epsilon}{\sigma_t} \cdot \nabla_{\theta} \mu_{\theta}(\mathbf{x}_t, t, \mathbf{c}) \quad (20)$$

Expanding $\nabla_{\theta} \mu_{\theta}(\mathbf{x}_t, t, \mathbf{c})$:

$$\nabla_{\theta} \mu_{\theta}(\mathbf{x}_t, t, \mathbf{c}) = \nabla_{\theta} \left[\frac{\sqrt{\alpha_{t-1}}}{\sqrt{\alpha_t}} \mathbf{x}_t - \frac{\sqrt{\alpha_{t-1}(1-\alpha_t)}}{\sqrt{\alpha_t}} \epsilon_{\theta}(\mathbf{x}_t, t, \mathbf{c}) + \sqrt{1-\alpha_{t-1}-\sigma_t^2} \cdot \epsilon_{\theta}(\mathbf{x}_t, t, \mathbf{c}) \right] \quad (21)$$

$$= \nabla_{\theta} \left[\left(\sqrt{1-\alpha_{t-1}-\sigma_t^2} - \frac{\sqrt{\alpha_{t-1}(1-\alpha_t)}}{\sqrt{\alpha_t}} \right) \epsilon_{\theta}(\mathbf{x}_t, t, \mathbf{c}) \right] \quad (22)$$

$$= \left(\sqrt{1-\alpha_{t-1}-\sigma_t^2} - \frac{\sqrt{\alpha_{t-1}(1-\alpha_t)}}{\sqrt{\alpha_t}} \right) \cdot \nabla_{\theta} \epsilon_{\theta}(\mathbf{x}_t, t, \mathbf{c}) \quad (23)$$

Let C_t denote the scalar coefficient in parentheses that varies with timestep t . Now, substituting the expansion of $\nabla_{\theta}\mu_{\theta}$ back into Eq. 20, we establish the direct relationship:

$$\nabla_{\theta} \log \pi_{\theta}(\mathbf{x}_{t-1}|\mathbf{x}_t, \mathbf{c}) = \underbrace{\frac{\epsilon}{\sigma_t}}_{K_t} C_t \cdot \nabla_{\theta} \epsilon_{\theta}(\mathbf{x}_t, t, \mathbf{c}) \quad (24)$$

Here, we have explicitly derived the coefficient K_t . Finally, we substitute this complete form into the LRPO gradient objective:

$$\nabla_{\theta} \mathcal{J}_{\text{LRPO}}(\theta) = \sum_{t=0}^{T-1} \mathbb{E}_{\mathbf{x}_T, \epsilon} \left[(K_t \cdot \nabla_{\theta} \epsilon_{\theta}(\mathbf{x}_t, t, \mathbf{c})) (w_t \cdot \hat{A}_t) \right] \quad (25)$$

$$= \sum_{t=0}^{T-1} \mathbb{E}_{\mathbf{x}_T, \epsilon} \left[(w_t K_t) \cdot \hat{A}_t \cdot \nabla_{\theta} \epsilon_{\theta}(\mathbf{x}_t, t, \mathbf{c}) \right] \quad (26)$$

This formally proves that our advantage weight, w_t , becomes part of a new scalar term ($w_t K_t$) that directly multiplies the network’s gradient, $\nabla_{\theta} \epsilon_{\theta}$. More importantly, this derivation reveals how our noise-level advantage assignment directly translates into a principled modulation of the learning signal at different stages of the denoising process. The final update to the network’s parameters θ is effectively scaled by our time-dependent weight. In the early stages of denoising, where the model needs to vigorously explore and establish the image’s overall structure and identity, our mechanism intelligently increases the optimization intensity. This encourages the policy to discover more diverse and high-quality solutions. Conversely, during the later stages, when the image is mostly formed and the task shifts to refining high-frequency details, our method reduces the optimization strength. This prevents large, disruptive updates from corrupting fine textures and ensures a more stable, fine-grained training process that converges smoothly.

B. Implementation details

Training Setup. We initialize our policy network with the official pre-trained weights of DiffBIR-v1¹, which was pre-trained on the FFHQ dataset. Our entire framework is built upon PyTorch 2.7.0. The training is conducted on three NVIDIA RTX 4090 GPUs and accelerated using the DeepSpeed library. A key component of our online training pipeline is a dedicated reward server, which is deployed on a separate NVIDIA RTX 4090 GPU to efficiently compute and provide reward signals to the policy network.

Hyperparameters. The policy network is optimized using the Adam optimizer with a learning rate of 1×10^{-6} and a batch-size of 6. For the denoising process, we employ the DDIM sampler. During training, we set $\eta = 1.0$ to introduce stochasticity that encourages exploration, while for inference, we use $\eta = 0.8$ to achieve more deterministic and stable generation. For our LRPO algorithm, we set the number of candidate samples per group to $G = 9$ and the policy update clipping range to 1×10^{-4} . The GT-guided likelihood regularization is weighted by a coefficient of $\alpha = 0.001$. Crucially, this regularization is only applied during the final $S = 5$ steps of the denoising process. This strategic application prevents the policy’s exploration from being overly constrained during the initial, more impactful stages of the reverse process.

C. Composite Reward Function Details

This section provides more details on the reward function, $R(\hat{\mathbf{x}}_0, \mathbf{x}_{\text{GT}})$. The function is engineered to deliver a holistic assessment of restored images by balancing human aesthetic preference, perceptual quality, and fidelity. The total reward score is a weighted aggregation of four components, formulated as:

$$R(\hat{\mathbf{x}}_0, \mathbf{x}_{\text{GT}}, \mathbf{c}_{\text{text}}) = 0.3 \cdot r_{\text{pref}} + 0.1 \cdot r_{\text{aq}} + 0.3 \cdot r_{\text{lpips}} + 0.3 \cdot r_{\text{dwt}}$$

where $\hat{\mathbf{x}}_0$ is the restored image, \mathbf{x}_{GT} is the ground-truth image, and \mathbf{c}_{text} is the textual description corresponding to \mathbf{x}_{GT} . We elaborate on each component below.

Human Preference Reward (r_{pref}). The human preference evaluation we use is based on the previous work [40], called the Face Reward Model. Trained on several human preference datasets, it is able to provide face restoration evaluations with high human consistency. The Face Reward Model’s input requires both $\hat{\mathbf{x}}_0$ and \mathbf{c}_{text} , the latter corresponding to the GT face.

¹The source code and weights from <https://github.com/XPixelGroup/DiffBIR>.

Perceptual Quality Reward (r_{aq}). This component, r_{aq} , offers a no-reference evaluation of the image’s absolute quality. We employ the CLIPIQA (CLIP-based Image Quality Assessment) metric [34] from the `pyiqa` library. It assesses overall perceptual quality and realism without requiring a reference image, making it effective for identifying artifacts.

Fidelity Reward (r_{fid}). The fidelity reward ensures the restoration remains faithful to the ground-truth. Our implementation uses a composite metric combining LPIPS to constrain perceptual similarity and a DWT-based measure for structural similarity.

LPIPS. The Learned Perceptual Image Patch Similarity (LPIPS) [50] metric computes the distance between two images in a deep feature space, which correlates well with perception. As LPIPS is a distance metric (lower is better), we convert it into a similarity reward (higher is better) via the transformation: $r_{\text{lpiips}} = 1.0 - \text{LPIPS}(\hat{x}_0, x_{\text{GT}})$.

DWT. To maintain consistency between the restored image and the GT image, we employ a Discrete Wavelet Transform (DWT) as a structural constraint. DWT extracts the low-frequency components of the restored image \hat{x}_0 and the GT image x_{GT} for the constraint. We leave the high-frequency components unconstrained to allow for more flexible restoration, reduce interference with high-frequency information, and make the generation more vivid. The detailed formulation is as follows:

$$L_{\text{DWT}} = \|\text{DWT}_{\text{LF}}(\hat{x}_0) - \text{DWT}_{\text{LF}}(x_{\text{GT}})\|_1$$

Finally, the L_{DWT} is converted into a reward score using an exponential decay function, which maps the non-negative loss to a score in the range (0, 1]:

$$r_{\text{dwt}} = \exp(-15 \cdot L_{\text{DWT}})$$

The scaling factor is an empirically chosen value.

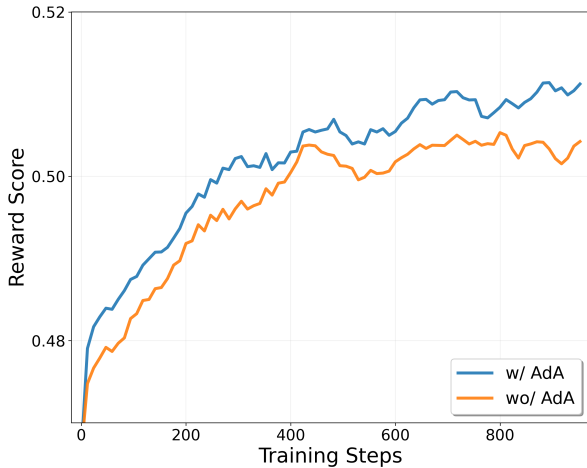


Figure 8. Reward scores during training w/ and w/o noise-level advantage assignment

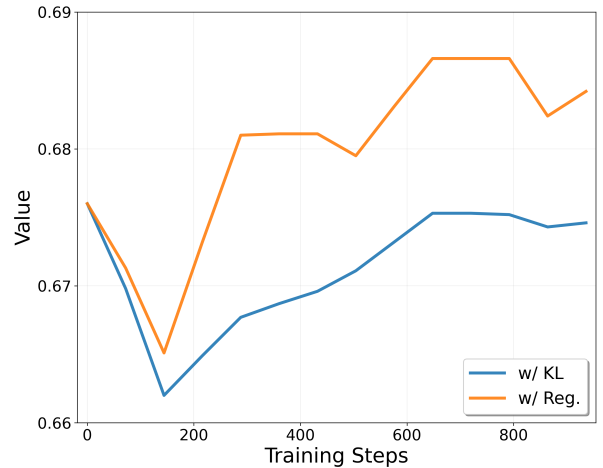


Figure 9. During RL training, the SSIM trend changes are compared between KL and Reg.

D. Ablation Study Details

We provide a more detailed explanation of the four variants presented in Table 4 of the main paper. In Table 4, Variant 2 employs the standard GRPO optimization objective, which includes the KL divergence term. Building upon this, Variant 1 removes the KL term from the optimization objective. While both Variant 3 and Variant 4 follow the GRPO training framework, Variant 3 integrates GT-guided likelihood regularization (Reg.), and Variant 4 integrates noise-level advantage assignment (AdA). Specifically, Variant 3 adds Reg. to the optimization term, with the advantage being assigned uniformly across the time steps. Variant 4 uses the suggested noise-level advantage assignment, but does not incorporate the Reg. term in the optimization objective.

Figure 8 and Figure 9 illustrate the differences in reward and SSIM scores when applying Ada and Reg strategies, respectively. Training dynamics in Figure 8 demonstrate that noise-level advantage assignment consistently outperforms uniform weighting, achieving superior reward scores and faster discovery of optimal restoration solutions. Additionally, Figure 9 validates replacing KL divergence with GT-guided regularization, as evidenced by improved SSIM convergence on CelebA-Test data, indicating better structural alignment with ground truth.

E. The Details of Human Preference Evaluation

To complement our quantitative metrics, we conducted a human preference evaluation to assess the perceptual quality and fidelity of our proposed LRPO against the DiffBIR. The study involved 12 participants from diverse backgrounds, each evaluating 100 randomly selected face restorations generated by both methods on the CelebA-Test dataset.

For each case, participants were shown the two restored images in a randomized order, along with the corresponding Ground Truth (GT) image for reference. They were then asked to make a forced-choice comparison, selecting one of the two images based on two independent criteria:

- *Realism*: Which image appears more natural and realistic, with richer facial details and fewer visual artifacts?
- *Fidelity*: Which restored face image is more consistent with the identity of the GT face?

Preference rates for realism and fidelity were independently calculated for both methods based on the collected responses. The final results, summarized in Table 3, show that our method was preferred by participants in terms of both realism and fidelity.

F. More Qualitative Results

This part shows more quantitative comparisons between our method and others. In Figure 11, we present additional comparison results between our method and others based on the synthetic dataset CelebA-Test.

In Figure 12, we present additional comparison results between our method and others based on the real-world datasets.

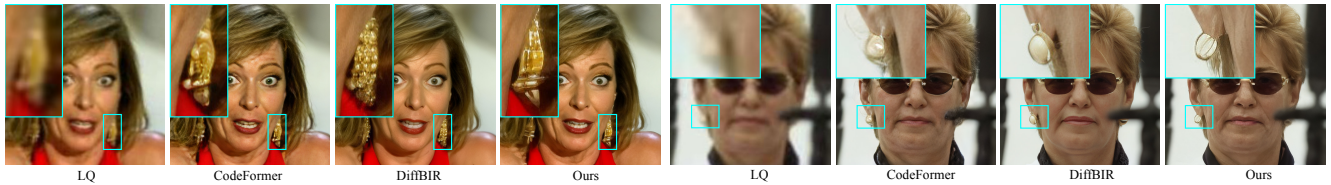


Figure 10. Failure cases. Restoration of highly rare specialized and individualized objects such as jewelry achieves suboptimal results.

G. Limitation.

Despite the improvements over existing approaches, our method is not without limitations. One failure case involves the restoration of highly individualized attributes, such as complex jewelry and accessories (Figure 10). Due to the limited representation of such rare objects in the training data of the base diffusion model, our method may fail to hallucinate plausible high-frequency details for these regions, occasionally resulting in blurred or distorted artifacts. Additionally, while the inference speed remains consistent with the base model, the training stage of LRPO requires additional computational resources for online sample generation and reward calculation compared to standard supervised fine-tuning. Future work aims to mitigate the artifact issue by exploring more diverse datasets and improving the efficiency of the RL alignment process.



Figure 11. Qualitative results on CelebA-Test datasets. (Zoom in for details)



Figure 12. Qualitative results on real-world datasets. (Zoom in for details)